A Highly Resolved Regional Climate Model (IPRC-RegCM) and Its Simulation of the 1998 Severe Precipitation Event over China. Part I: Model Description and Verification of Simulation[*]

YUQING WANG, OMER L. SEN, AND BIN WANG

International Pacific Research Center, School of Ocean and Earth Science and Technology, University of Hawaii at Manoa, Honolulu, Hawaii

(Manuscript received 6 June 2002, in final form 22 November 2002)

ABSTRACT

East Asia is a region with complex topography, land surface conditions, coastlines, and with large contribution from mesoscale phenomena, such as the mei-yu/baiu frontal systems and tropical storms. To study the regional climate in such a region, a highly resolved regional climate model (IPRC-RegCM) has been recently developed at the International Pacific Research Center (IPRC). The distinct features of this model include the direct feedback of cumulus detrained cloud ice and cloud water into the grid-resolved quantities; the effect of cloud buoyancy on turbulence production with mixed-ice phase clouds; an explicit coupling between the cloud microphysics and radiation via cloud properties; an explicit coupling between land surface and radiation via surface albedo, direct and diffuse radiation fluxes; and the effect of frictionally generated dissipative heating.

The model is documented in detail and the performance of the model is demonstrated by its simulation of the 1998 severe flooding event over China, the worst one since 1955. With the use of the objective analysis of the European Centre for Medium-Range Weather Forecasts (ECMWF), which is available at 12-h intervals with a resolution of 2.5° × 2.5°, as both the initial and lateral boundary conditions, the model was integrated from 26 April to 31 August 1998 with a resolution of 0.5° × 0.5° covering the area 5°–45°N, 90°–140°E. The model simulated realistically not only the temporal evolution of the area-averaged precipitation and the monthly mean precipitation spatial pattern but also the daily precipitation intensity distribution. The model reproduced the monsoon circulations, in particular, two episodes of the intraseasonal oscillation events that are believed to be closely related to the unusual double mei-yu periods over the Yangtze River basin in 1998.

1. Introduction

Regional climate models have been increasingly used in climate research (e.g., Dickinson et al. 1989; Giorgi 1990; McGregor and Walsh 1994; Jones et al. 1995; Christensen et al. 1997; Caya and Laprise 1999). The principle behind the regional climate model technique is that, given a large-scale atmospheric circulation, a limited-area model with a suitably high-resolution resolving complex topography, land–sea contrast, land use, and detailed description of physical processes can generate realistic high-resolution (both spatial and temporal) information coherent with the driving large-scale circulation supplied by either reanalysis data or a global general circulation model (GCM). The regional climate

modeling has been proven to be able to improve simulation of regional scales with great details, especially in the region where forcing due to complex topographical effect or coastlines, or both, regulate the regional distribution of climate variables (e.g., Giorgi 1990; Jones et al. 1995; Walsh and McGregor 1995; Renwick et al. 1998; Wang et al. 2000). The regional climate modeling approach has also been shown to be useful for improving our understanding of many climate processes, such as cloud–radiation forcing, cumulus convection, and land surface processes, etc. (e.g., Pan et al. 1995; Paegle et al. 1996; Giorgi et al. 1996; Dudek et al. 1996; Bosilovich and Sun 1999; Schär et al. 1999; Pal and Eltahir 2001). Comprehensive reviews on the regional climate modeling can be found in Giorgi and Mearns (1991, 1999), McGregor (1997), and more recently in the third assessment report of the International Panel on Climate Change (IPCC; Houghton et al. 2001).

Although significant progresses have been made in the last decade or so in the area of the regional climate modeling, there remain many discrepancies in the current regional climate models. The most common problem, as reviewed by McGregor (1997), is the relatively low skill in simulating the regional climate in the Trop-

ics. There are two major factors that are responsible for this difficulty: one is the dominated cumulus convection in the Tropics, which seems not to be represented well by current regional climate models, and the other is the much weaker large-scale forcing in the Tropics than that in the mid- and high latitudes. This latter could produce accumulation of errors in the interior model domain and thus affect the long-term simulation of regional climate in the Tropics.

Another major uncertainty of current regional climate models is the treatment of clouds, a critical weakness that needs improvement in both global and regional climate models (e.g., Giorgi and Mearns 1999). Although the detailed explicit cloud microphysics parameterization for grid resolved moist processes is considered in some of the regional climate models, the complex interaction between subgrid cumulus convection and grid-scale moist processes is very crudely treated. Some studies have indicated the improvements in radiation budgets by using cloud microphysics information either in column models (Petch 1998) or in the GCM (Fowler and Randall 1996), but the cloud amount is treated in a quite simple way and is usually estimated by the relative humidity in most global and regional climate model applications (e.g., Giorgi et al. 1993a; Dudek et al. 1996; Wang et al. 2000). One exemption is Hong et al. (1998), who used the prognostic cloud scheme with Randall's (1995) cloud fraction scheme, which accounts into not only the relative humidity but also the cloud condensates, in the National Centers for Environmental Prediction regional spectral model (RSM).

In addition, as indicated in the IPCC 2001 report (Houghton et al. 2001) previous studies have shown the capability of regional climate models in reproducing interannual variability when driven by good quality driving fields. However, more analysis and improvements are needed of model performance in simulating climate variability at short timescales (daily to subdaily). In particular, the increased resolution of regional climate models can allow simulation of a broader spectrum of weather events to improve simulation of the daily precipitation intensity distributions. Such a skill is extremely important to give confidence of the model-simulated climate sensitivity or climate change scenarios. Another area IPCC recommended is the need to coordinate regional climate modeling efforts and to extend studies to more regions and to perform ensemble simulations with different models.

At the International Pacific Research Center (IPRC), efforts have been made to develop a highly resolved regional climate model, aiming at simulating variability of Asian–Australian monsoon system and assessing impacts of the global change on the Asian–Pacific climate (Wang and Wang 2001). The overall goal is to realistically simulate regional and mesoscale features of the Asian–Australian monsoon system and associated hydrological cycle. The Asian–Pacific monsoon has many unique features. For instance, the mei-yu/baiu is known

for its narrow meridional scale and organized mesoscale convective systems, which differ from those seen in the other regions of the world (e.g., Ding 1994; Chen et al. 1998). To realistically simulate the mei-yu/baiu system poses a great challenge for existing GCMs (e.g., Kang et al. 2002) and regional climate models (Kida et al. 1991; Liu et al. 1994, 1996; Hong et al. 1999; Leung et al. 1999; Sasaki et al. 2000). Simulation of monsoon circulation with GCMs was found to be very sensitive to different cumulus parameterization schemes (Zhang 1994). Modeling studies with regional climate models also indicated that some cumulus parameterization schemes do not seem to work well in the East Asian monsoon region (Leung et al. 1999; Lee and Suh 2000). The western Pacific monsoon involves heavy activity of tropical storms; the collective effects of these transient storms have considerable contribution to the monthly and seasonal mean climate. Scale interactions are extremely complex in the Asian–Pacific monsoon region (Holland 1995), which are further complicated due to the effects of Tibetan plateau, land surface processes, ocean–continent contrast, and air–sea interaction associated with storms. These specific features require special consideration in designing regional climate models to be used in this particular region.

Our overall goal thus is to develop a highly resolved regional climate model that will be imbedded within a global coupled atmosphere–ocean–land model, serving as a primary tool for studies of climate processes, climate change impact, and short-term climate prediction for (but not limited to) the Asian–Australian monsoon system. The objectives of this paper are twofold: to describe the numerical model that we have developed in the last 2 yr and to demonstrate the ability of the model in simulating severe climate events over East Asia. The next section describes the numerical model developed. Section 3 gives a brief description of the 1998 severe precipitation event over East Asia. Design of the numerical experiment is given in section 4. The simulation result of this extreme precipitation event and the associated circulation is discussed in section 5. Concluding remarks are presented in the last section.

2. Description of the IPRC-RegCM

The regional climate model developed at the IPRC (hereafter IPRC-RegCM) was initially based on the high-resolution tropical cyclone model (TCM3) previously developed by the first author (Wang 1999, 2001, 2002a). A detailed description of TCM3 and its performance and capability of simulating scale interactions in tropical cyclones can be found in Wang (2001, 2002a,b,c). Since TCM3 was originally developed for idealized high-resolution modeling studies of tropical cyclones over the ocean, accurate radiation budget, subgrid cumulus parameterization scheme, and land surface processes were not included in TCM3. However, these are critical to realistic simulation of climate. In order

to facilitate climate research, we not only implemented an advanced radiation package (Edwards and Slingo 1996; Sun and Rikus 1999), a common land surface scheme (Biosphere–Atmosphere Transfer Scheme; Dickinson et al. 1993), and a mass flux cumulus parameterization scheme (Tiedtke 1989; Nordeng 1995), but also considered several detailed feedback processes in the climate system, such as the direct interaction between clouds, radiation, and land surface; interaction between subgrid and grid-resolved cloud processes, effect of cloud buoyancy on turbulence production, and inclusion of dissipative heating. With these implementations and some new development, the model has been made to be suitable for climate research.

The model uses hydrostatic primitive equations in spherical coordinates with σ (pressure normalized by surface pressure) as the vertical coordinate. To facilitate long-term integration with high accuracy, the model uses a fourth-order advective conservative finite-difference scheme (Xue and Lin 2001) on an unstaggered longitude–latitude grid system and a second-order leapfrog scheme with intermittent use of Euler backward scheme for time integration. The model has 28 levels in the vertical with substantial concentration of resolution in the planetary boundary layer. The model physics are carefully chosen based on the up-to-date developments.

The comprehensive cloud microphysics scheme developed by Wang (1999, 2001) is used in the model to represent the grid-scale moist processes. Prognostic variables in this scheme include mixing ratios of water vapor, cloud water, rainwater, cloud ice, snow, and graupel. Cloud water is assumed to be monodispersed and to move with the air, while cloud ice is monodispersed but precipitates with the terminal velocity given by Heymsfield and Donner (1990). Condensation/evaporation of cloud water takes place instantaneously when the air is supersaturated/subsaturated. There are in total 36 different cloud microphysical processes that are considered in our cloud microphysics scheme (see Wang 1999, 2001 for details).

Subgrid convective processes, such as shallow convection, midlevel convection, and penetrative deep convection, are considered based on the mass flux cumulus parameterization scheme originally developed by Tiedtke (1989), and later modified by Nordeng (1995). This modified version uses a convective available potential energy closure instead of the previous moisture convergence closure and considers the organized entrainment and detrainment based on a simple cloud plume model. In our implementation, the detrained cloud water/ice at the top of cumulus tower are not instantaneously evaporated as used in the original scheme of Tiedtke (1989) but returned to the grid-scale cloud water/ice as treated in the ECHAM4 GCM (developed at the Max Planck Institute for Meteorology in Germany; Roeckner et al. 1996). Partitioning between cloud water and cloud ice of the detrained condensates above the freezing level ($T < T_0 = 273.16$ K with T the ambient air temperature) is a function of temperature given by Rockel et al. (1991). The liquid fraction is thus given by

$$f_{liq} = a + (1 - a)e^{-b(T-T_0)^2}, \tag{1}$$

with $a = 0.0059$ and $b = 0.003\,102$, while $f_{liq} = 1$ for $T \geq T_0$. As a result, the ice fraction is given by $f_{ice} = 1 - f_{liq}$. To prevent deep convection occurring in dry regions, a threshold value RH_c is set for the vertically averaged relative humidity between the cloud top and cloud base $\overline{RH}$. Deep convection is allowed to occur only when $\overline{RH} \geq RH_c$ (=0.8 in our application) in the detected cloud column.

The subgrid-scale vertical mixing is accomplished by the so-called E-ϵ turbulence closure scheme in which both turbulent kinetic energy and its dissipation rate are prognostic variables (Detering and Etling 1985). In our application, we have included both advection processes and the effect of moist-adiabatic processes with mixed-ice phase in cloudy air on the buoyancy production of turbulence (Wang 1999). Turbulent fluxes at the ocean surface are calculated using the modified Monin–Obukhov scheme—the Tropical Ocean Global Atmosphere Coupled Ocean–Atmosphere Response Experiment (TOGA COARE) algorithm (Fairall et al. 1996). Turbulent fluxes over the land surface are calculated based on the bulk aerodynamic method used in the land surface scheme (see below). Dissipative heating due to molecular friction in the planetary boundary layer is considered to conserve the internal energy of the atmosphere. Different from Bister and Emanuel (1998), we considered only the dissipative heating related to turbulence kinetic energy dissipation rate (ϵ), which is a prognostic variable in our model.

To facilitate climate research and to realistically simulate the cloud–radiation feedback, the radiation package originally developed by Edwards and Slingo (1996) and further improved later by Sun and Rikus (1999) is used in the model. This radiation scheme includes seven/four bands for longwave/shortwave radiation calculations. Both shortwave and longwave scatterings are considered. In our implementation, surface albedos of diffuse and direct radiations calculated in the land surface model are directly used in determining the shortwave radiation in the radiation budget. We also considered a full coupling between the cloud microphysics and the cloud optical depth required in the radiation calculation. Cloud optical properties are based on Sun and Shine (1994) for longwave radiation, while based on Slingo and Schrecker (1982) and Chou et al. (1998) for shortwave radiation. Both climatological ozone with seasonal cycle and constant mixing ratio of carbon dioxide for the present climate are considered in the radiation budget.

Cloud amount is not a prognostic variable in the model at present, rather it is diagnosed using the semiempirical cloudiness parameterization scheme developed

by Xu and Randall (1996) based on the results from cloud-resolving model simulations. By this scheme, the cloud amount (C_a) is determined by both relative humidity and cloud water–ice mixing ratio,

$$C_a = \begin{cases} \mathrm{RH}^p\{1 - e^{-(\alpha_0 q_l)/[(1-\mathrm{RH})q^*]^\gamma}\}, & \text{if RH} < 1; \\ 1, & \text{if RH} \geq 1 \end{cases} \quad (2)$$

where p, γ, and α_0 are constants and taken to be 0.25, 0.49, and 100, respectively; $q_l = q_c + q_i$ is the total mixing ratio of cloud water (q_c) and cloud ice (q_i); q^* is the mass-weighted saturated water vapor mixing ratio and is defined as

$$q^* = f_c q_{sw} + f_i q_{si}, \quad (3)$$

where $f_c = 1 - f_i$; q_{sw} and q_{si} are, respectively, the saturated mixing ratio with respect to water and ice surfaces; and

$$f_i = \begin{cases} 1, & \text{if } T \leq T_{fr} \\ q_i/(q_c + q_i), & \text{if } T_{fr} < T < T_0; \\ 0, & \text{if } T \geq T_0, \end{cases} \quad (4)$$

where $T_{fr} = 233.15$ K is the temperature at which a homogeneous freezing occurs. Note that the relative humidity RH in (2) is calculated based on the mass-weighted saturated mixing ratio here.

To include the land surface processes, the Biosphere–Atmosphere Transfer Scheme (BATS) developed by Dickinson et al. (1993) was coupled with the atmospheric model by a semi-implicit coupling algorithm (Polcher et al. 1998). BATS incorporates one canopy and three soil layers, and it requires land cover/vegetation (18 types), soil texture (12 types), and soil color (8 types) maps for spatial applications as in a GCM. In our application, these datasets were obtained from the U.S. Geological Survey (USGS; second version of USGS 1-km resolution land cover classification dataset), the U.S. Department of Agriculture (global 10-km soil data). Soil water contents were initialized using a method described by Giorgi and Bates (1989) such that the initial values depend on the vegetation and soil type defined for each grid cell. As mentioned earlier, surface albedo components corresponding to the diffuse and direct shortwave radiation components estimated in BATS are passed to the radiation routine and used for shortwave radiation calculation.

In our implementation of BATS, we found that the iteration to solve leaf energy balance equation may not converge in some occasions, such as when strong convective rain develop between two radiation calculation time steps (that is 1-h in our current application). The rain that falls on the leaf surface when the shortwave radiation is high produces large evaporation rates and therefore substantial cooling on the surface. If this cooling is large enough, it might change the surface layer from unstable to stable in the next iteration. Because the surface fluxes are limited by the stability of the

surface layer, the iteration could fail to converge to a reasonable leaf temperature in few extreme cases when the limited surface flux could not balance the high shortwave radiation. This problem happens at few grid points and at few time steps, and thus does not have a noticeable effect on the model climatology except for the development of some short-lived gridpoint storms. To avoid this problem, a simple algorithm has been developed that prevents large fluctuations in leaf temperature by only allowing it to change gradually from one iteration to the next. The iteration process is thus slowed down but the convergence is assured for all cases.

A fourth-order horizontal diffusion is applied on σ surfaces for all prognostic variables except for surface pressure. The horizontal diffusion coefficients in zonal (K_{Hx}) and meridional (K_{Hy}) directions are different, and are given, respectively, by

$$K_{Hx} = A_x \left[b K_{Hx0} + \frac{1}{2} k^2 (a\Delta\lambda \cos\varphi)^2 |D| \right],$$

$$K_{Hy} = A_y \left[b K_{Hy0} + \frac{1}{2} k^2 (a\Delta\varphi)^2 |D| \right], \quad (5)$$

where $K_{Hx0} = 0.8 a\Delta\lambda \cos\varphi$ and $K_{Hy0} = 0.8 a\Delta\varphi$ are background values, respectively, in zonal and meridional directions; a the radius of the earth; $\Delta\lambda$ and $\Delta\phi$ grid spacing in longitude and latitude directions, respectively; $|D|$ the deformation of horizontal wind; and $k = 0.4$ the von Kármán constant. In (5), $b = \sqrt{(nb - n + 1)}$, where $n = 1, 2, 3, \ldots, nb$, is the number of grid points normal to the lateral boundaries, nb is taken to be 16 in the model. This increased linear part of the diffusion coefficient is used to suppress any noise possibly generated near the lateral boundaries. The A_x and A_y in (5) are functions of topographic slopes in zonal and meridional directions and are given by

$$A_x = \frac{d}{d + [c(\partial H_s/\partial\lambda)/(a\cos\varphi)]^2};$$

$$A_y = \frac{d}{d + [c(\partial H_s/\partial\varphi)/a]^2}; \quad (6)$$

where, d, c are two constants and given as 1.0 and 10^2, respectively; H_s is the model topographic height. In comparison with that used by Giorgi et al. (1993b), who used the same reduction factor for both zonal and meridional directions, the use of (5) with (6) gives reduced horizontal diffusion only in the direction normal to the topographic slope, and thus is more selective to damp computational mode near the steep topographic area.

The regional model can be run with both initial and lateral boundary conditions from either global analysis/reanalysis data or the output of a GCM. As most of other gridpoint regional climate models, a one-way nesting is used to update the model time integration in a buffer zone near the lateral boundaries within which the model prognostic variables are nudged to the reanalysis
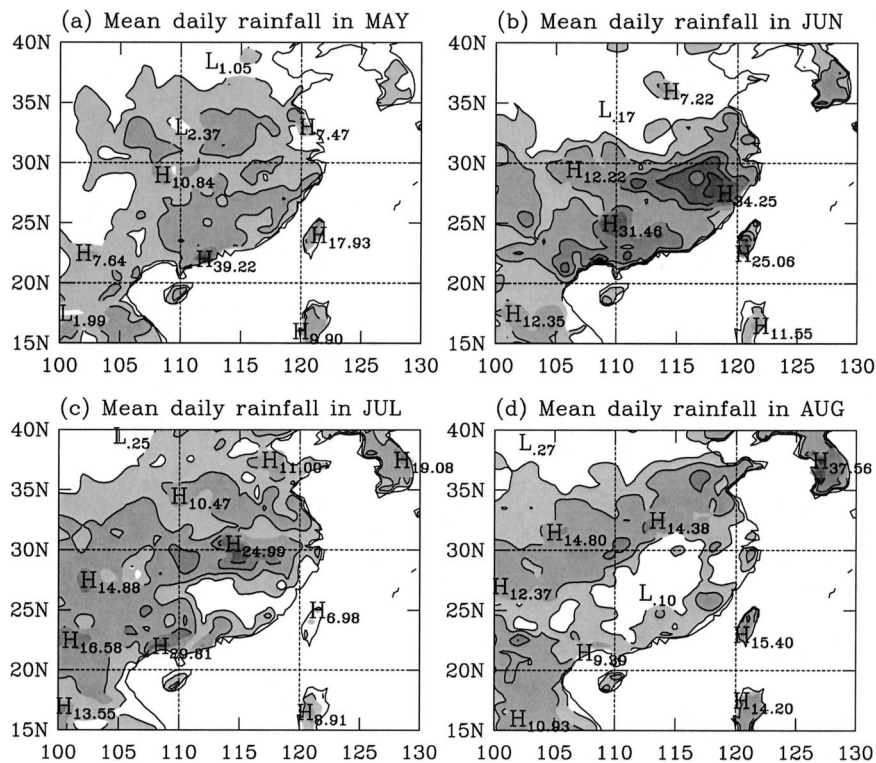
FIG. 1. Distribution of observed monthly mean daily rainfall over the East Asian continent in the 4 months from May to Aug in 1998. Contours are shown at 3, 6, 12, 18, 24, and 30 mm day^{-1}.

data or the GCM results with an exponential nudging coefficient proposed by Giorgi et al. (1993b) and later modified by Liang et al. (2001). The nudging coefficient is given by

$$F = \text{Min}[1, (L - n)/(L - 2)e^{-(n-1)/m}], \qquad (7)$$

where L is the total grid points in the buffer zone, n the index of grid points normal to the lateral boundaries, and m is a function of height and given by

$$m = \text{Max}[3, 3 + 2(0.85 - \sigma)], \qquad (8)$$

where σ is the model vertical coordinate. This gives larger nudging coefficients at higher levels to increase the large-scale control by the driving fields, as used in many other applications (e.g., Giorgi et al. 1993b; Liang et al. 2001). Since we prefer to use a relatively large model domain, the width of the buffer zone in our model is set to be $L = 21$.

As used in Giorgi et al. (1993b), an inflow–outflow boundary condition is used for water vapor mixing ratio but with a very weak nudging in the buffer zone (with a nudging coefficient 1% of that for surface pressure, wind, and temperature) to prevent the moisture field drifting away from the driving fields. Since there are no hydrometeor fields provided by the driving fields, we simply set mixing ratios of cloud water, rainwater, cloud ice, snow, and graupel to be zero at inflow boundaries, while they are advected outward at the outflow bound-

aries. This outflow boundary condition is also used for both turbulent kinetic energy and its dissipation rate.

Note that we do not calculate the physical tendency at each time step of dynamical core, but every 60 min for radiation while 12 min for all other physical processes. During the period of every 60 min, the radiation tendency is linearly interpolated to every 12 min in time. However, during every 12 min, the physical tendency is kept unchanged when the dynamical core is updated with small time steps (using a time step of 72 s, with $0.5° \times 0.5°$ latitude–longitude resolution in our standard settings).

3. An overview of the 1998 severe precipitation event over China

During the monsoon/mei-yu season in 1998, a severe flooding event occurred in the Yangtze River basin ($26°$–$32°N$, $110°$–$122°E$; Fig. 1) that was the worst event recorded since 1955 brought about large economic losses in China. This severe flooding event was induced by severe precipitation events associated with the activities of the summer monsoon and mei-yu fronts over East Asia (Ding and Liu 2001). The abnormal monsoon rainfall was also related to the prolonged impact of the strongest 1997/98 El Niño event in the last century (Ding and Liu 2001).

Since a full description of the 1998 East Asian summer monsoon and severe precipitation event over China
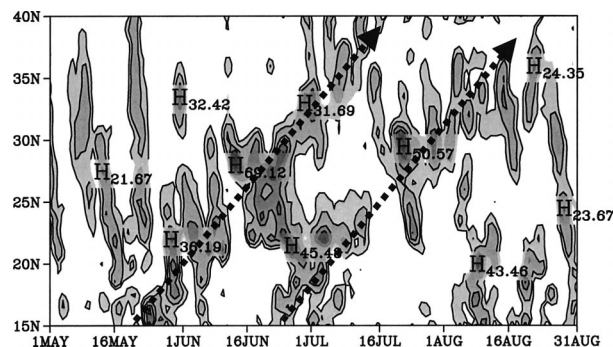
FIG. 2. Time–latitude cross section of daily precipitation (mm day^{-1}) averaged between 105° and 122°E from 1 May to 31 Aug in 1998 based on distributed rainfall from station data. Thick dashed arrows indicate the northward-propagating intraseasonal events. Contours are shown at 5, 10, 20, . . . , and 60 mm day^{-1}.
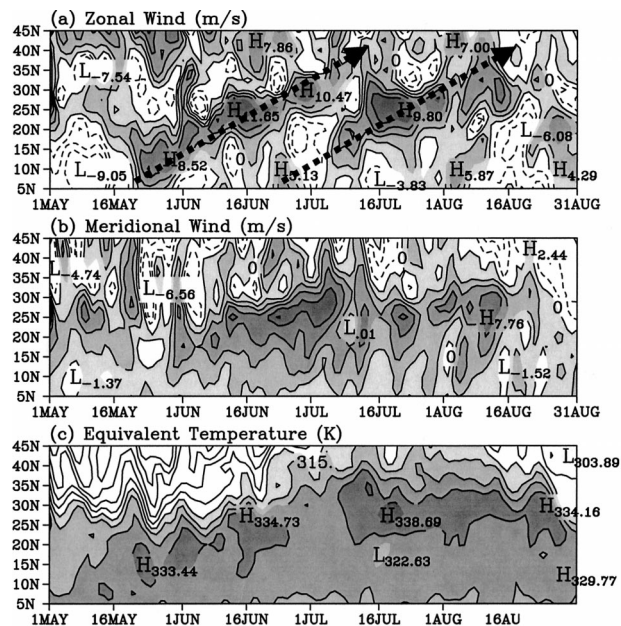

FIG. 3. Time–latitude cross section of (a) zonal wind, (b) meridional wind, and (c) equivalent temperature at 850-hPa averaged between 110° and 120°E from ECMWF analysis. Units are m s^{-1} for winds and K for equivalent temperature. Contour intervals are 2 m s^{-1} for winds and 5 K for equivalent temperature. Thick dashed arrows in (a) indicate the northward-propagating intraseasonal events.

can be found in Ding and Liu (2001), only some major features of the monsoon activities and their relationship to the severe precipitation events are highlighted here. The three significant episodes of severe rainfalls/floods in China (Fig. 2) were related to the East Asian monsoon activities (Fig. 3). Westerlies first appeared over the northern part of the South China Sea (SCS, around 15°–20°N) in middle May and were triggered by a cold frontal system and the associated rainfall from midlatitudes (Figs. 2 and 3a). From mid-May, the westerlies extended southward and occupied the whole SCS (Fig. 3a), with concentrated rainfall over south China (Fig. 2), as also seen from the equivalent temperature[1] (Fig. 3c), and thus the onset of East Asian monsoon over the SCS (Ding and Liu 2001).

From later May and early June, the monsoonal westerlies and southwesterlies moved northward and prevailed over south China (20°–25°N) and the region to the south of the Yangtze River (25°–30°N), consecutively, thus marking onset of the summer monsoon over the extensive region south of the Yangtze River (the region south of 30°N, Fig. 3). On around 10 June, the monsoon flow strengthened and rapidly progressed to the region south of the Yangtze River (25°–30°N) and persisted there until the end of June (Fig. 3), concurring with the first severe flooding event during the normal mei-yu period in the Yangtze River basin (Fig. 2). During the week of late June to July 4, the monsoonal westerly–southwesterly circulation strengthened and propagated farther northward, with its leading edge spreading to the Huaihe River basin (30°–35°N, Fig. 3) and with the associated major rainbelt rapidly moving to the Huaihe River basin (30°–35°N, Fig. 2). The monsoon suddenly retreated to the Yangtze River basin in

middle July after a short visit over north China from 5 to 16 July (Fig. 3), thus bringing about the unusual second mei-yu period and heavy rainfall and severe floods over the Yangtze River basin (Fig. 2), in contrast to the normal dry summer season in this region (Wang and LinHo 2002). The double mei-yu periods thus caused extensively heavy rainfalls and severe floods in Yangtze River basin in 1998.

Note also that there were two northward-propagating intraseasonal oscillation (ISO) events visible during the monsoon season over East Asia. The first event originated from the equatorial region around later May with southwesterly flow (Figs. 3a,b) and rainfall propagating northward at a phase speed of around 0.7–0.9° latitudes per day. The northward propagation exhibited two stepwise jumps at about 22° and 30°N, occurring around 10 and 24 June, respectively. Such a stepwise northward-propagating ISO event appeared to be a salient feature associated with the evolution of the East Asian summer monsoon (Ding 1994; Wang and Xu 1997). The second ISO event originated in early July over SCS and propagated northward with a phase speed similar to the first event, as seen from both the zonal wind (Fig. 3a) and the daily rainfall (Fig. 2). This second event weakened in rainfall during middle July when a rainfall event moved southward from the higher latitudes. The westerly associated with this second ISO event merged with the retreated monsoon westerly in the Yangtze River basin, causing the second flooding event in this region. The second ISO event continued to progress northward

---

[1] Here, the equivalent temperature is defined as $T_e = T + L_v q / C_p$, where T is the air temperature, L_v the latent heat, q the mixing ratio of water vapor, C_p the specific heat at constant pressure. The mei-yu/baiu front and the associated rainbelt are mainly in the region with low-level high equivalent temperature as seen from Fig. 2c.
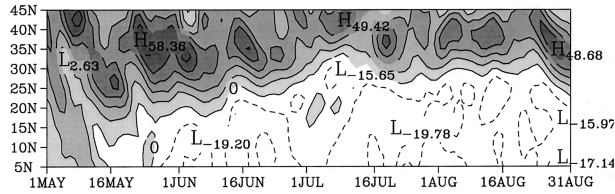
FIG. 4. As in Fig. 3a but for zonal wind at 200 hPa with contour interval of 10 m s^{-1}.

with its associated rainfall moving up to 37°N until middle August (Fig. 2). The period between the two ISO events was about 30 days with a wavelength of about 12° latitudes, as seen from the time–latitude section of daily rainfall shown in Fig. 2. The above analysis revealed that the monsoon rainfall over East Asia was largely regulated by the ISO. Therefore, further research on this aspect would improve both our understanding and prediction of monsoon rainfall.

In the upper troposphere at 200 hPa, in the early May (1–13 May), there was an upper-level westerly jet stream intruding southward from the middle latitudes (Fig. 4). This upper-level westerly jet stream was responsible for the outbreak of a cold frontal system southward in the lower troposphere and the southward propagation of the frontal rainfall as seen from Fig. 2. The activity of this frontal system triggered rainfall near the south coastal region of China and the low-level westerly flow and the onset of summer monsoon in the northern part of SCS. Associated with the SCS monsoon onset was a northward retreat and intensification of the upper-level westerly jet stream (Fig. 4). This upper-level westerly jet stream moved gradually northward during 22 May and 7 July and reached its most northward latitude of about 40°N (Fig. 4). This is consistent with the northward shift of monsoon rainfall (Fig. 2). During the third pentad of July, the upper westerly jet stream shifted southward as the second mei-yu period developed in the Yangtze River basin and then remained between 35° and 40°N until late August when it rapidly intruded southward, a signal of the withdrawal of the East Asian summer monsoon in 1998.

4. Experimental design

The IPRC-RegCM described in section 2 was used to simulate the 1998 severe precipitation event over East Asia as described in section 3 to evaluate the performance of the model. The European Centre for Medium-Range Weather Forecasts (ECMWF) global analysis data available at 12-h intervals with a resolution of 2.5° × 2.5° in the horizontal and 15 pressure levels up to 10 hPa were used to define the driving fields, which provide both initial and lateral boundary conditions to the regional climate model. Sea surface temperatures (SSTs) over the ocean were obtained from the Reynolds weekly SST data with horizontal resolution of 1° × 1° (Reynolds and Smith 1994), which were interpolated
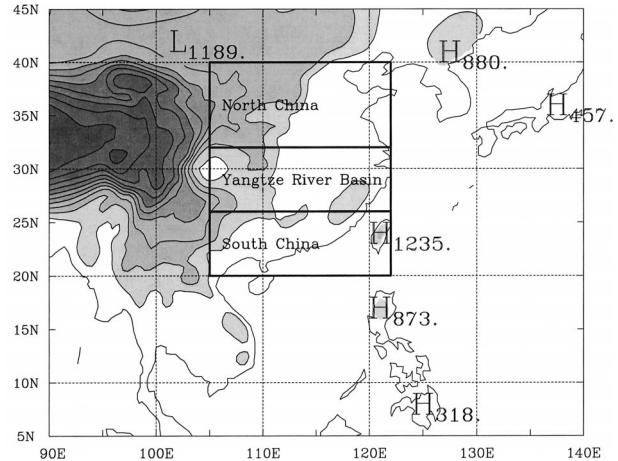

FIG. 5. Model topography in meters obtained based on the USGS high-resolution dataset with contour interval of 500 m. Three rectangular areas show three regions that will be used for areal averaging later. South China: 20°–26°N, 105°–122°E; Yangtze River basin: 26°–32°N, 105°–122°E; and north China: 32°–40°N, 105°–122°E.

into the model grids by cubic spline interpolation in space and linearly interpolated in time. Over the land, the initial surface soil and canopy temperatures were obtained from the lowest model level with a standard lapse rate of 6°C km^{-1}. Initial snow depths were set to be zero, while the soil moisture fields were initialized such that the initial soil moisture depends on the vegetation and soil type defined for each grid cell (Giorgi and Bates 1989).

The model domain was defined in the area of 5°–45°N, 90°–140°E (Fig. 5) with horizontal grid spacing of 0.5°, thus including 101 × 81 grid points. The USGS high-resolution topographic dataset (0.0833° × 0.0833°) was used to obtain the model topography. We first calculated the averaged topographic height within the model grid box (0.5° × 0.5°) using the USGS data and then added the standard deviation to the averaged value to get the envelope topography for this grid box (Fig. 5). The high-resolution vegetation type data from USGS is reanalyzed for the model based on dominant vegetation type in each grid box. The model was initialized from 0000 UTC on 26 April 1998 and integrated continuously through 31 August. The first 5 days were used for model spin up, therefore, our analyses will focus on the 4 months between 1 May and 31 August 1998.

The simulation results were compared with both the driving fields and the independent station data available for the model domain. Statistics similar to those used by Giorgi et al. (1993a,b) and Wang et al. (2000) were utilized to assess the different aspects of the model performance, including model bias from the observations, temporal correlation coefficient, and spatial pattern correlation coefficient between the model simulation and observation, and spatial standard deviation (see appendix). In addition, we also compared the modeled and observed frequency distributions of severe precipitation
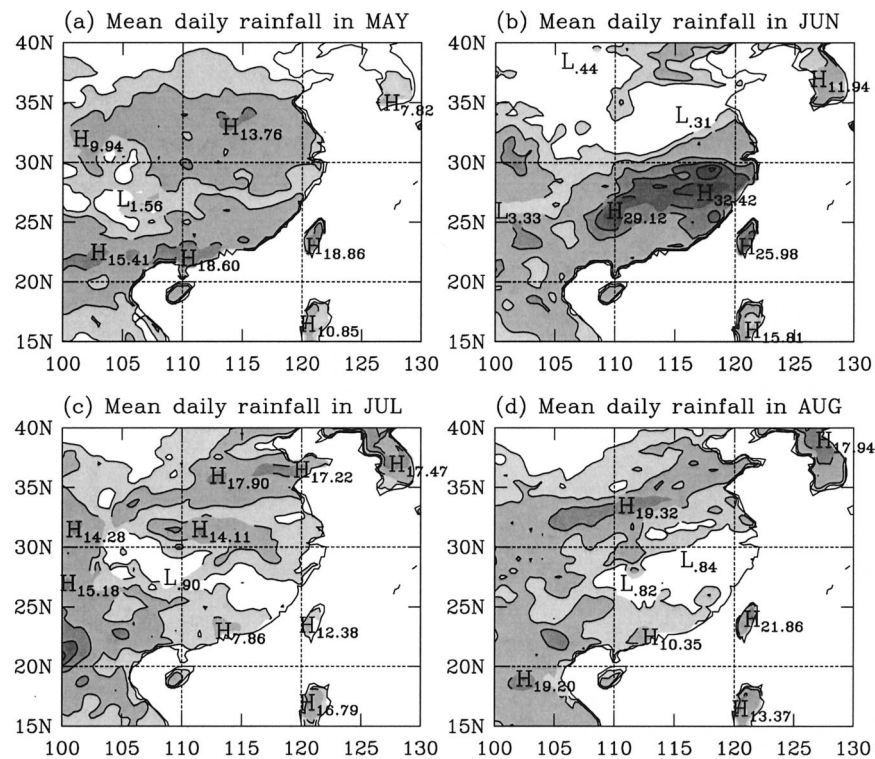
FIG. 6. Distribution of model-simulated monthly mean daily rainfall in the 4 months over the East Asian continent from May to Aug in 1998. Contours are the same as in Fig. 1.

events to examine the model's capability of simulating frequency of occurrence of extreme weather events. Before calculation of objective statistics, all the station data (such as the daily precipitation, 2-m height daily maximum, minimum temperatures, and relative humidities) were distributed to the model grid system by the triangle-based cubic spline interpolation algorithm.

5. Simulation results

a. Precipitation

The simulated monthly mean daily rainfalls in the 4 months from May to August 1998 are given in Fig. 6. The model simulated the overall spatial distributions of monthly mean rainfall (comparing Figs. 1 and 6). In May (Figs. 1a and 6a), the model simulated the distribution of monthly mean precipitation over southern China (south of 30°N) except for an underestimation of precipitation near the south coast. The precipitation over south China was related to the activities of two cold frontal systems that preluded the summer monsoon onset in the northern part of SCS in the first half of May and the summer monsoon activity in the second half of the month (section 3). In the northern part of China (north of 30°N), however, the model overestimated the precipitation. This overestimation resulted from the simulated too strong frontal rainfall in the region, probably related to the soil moisture initialization that favors

higher moisture values. In June (Figs. 1b and 6b), the model successfully reproduced the extensive severe precipitation in the Yangtze River basin (25°–30°N, 110°–122°E) except for a slightly southwest extension of heavy precipitation. The precipitation center around 25°N, 110°E in the observation was also well simulated. The model, however, underestimated precipitation to the west of 110°E along 30°N and overestimated precipitation to the north of 36°N between 110° and 120°E. In July (Figs. 1c and 6c), the precipitation around the Yangtze River basin along 30°N was considerably underestimated and was displaced to the north by about 2° latitudes in the simulation. This indicates that the second mei-yu period was not well simulated, especially in the second half of the month (section 3). However, the model well simulated both wet and dry conditions in the north China region and in the southeast part of China, respectively. The latter region was under control by the subtropical high-pressure system over the western North Pacific (not shown). In August (Figs. 1d and 6d), the observed major precipitation belt shifted to northern China and elongated from northeast to southwest (Fig. 1d). The model reproduced this precipitation belt reasonably well except for an underestimation of precipitation along the southeast coast of China (Fig. 6d).

In addition to realistic simulation of the spatial distribution of monthly mean precipitation discussed above, the model also simulated the temporal variation
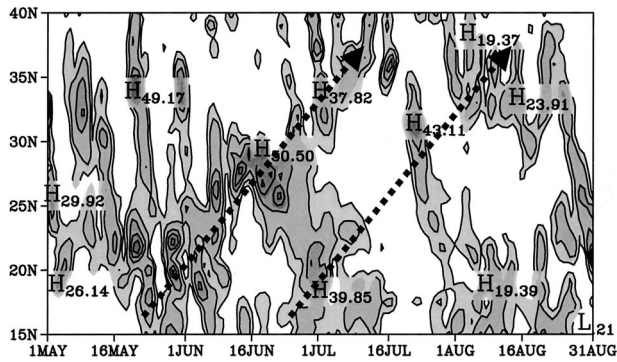
FIG. 7. Time–latitude cross section of daily precipitation (mm day^{-1}) averaged between 105° and 122°E from 1 May to 31 Aug in 1998 from model simulation. Thick dashed arrows indicate the northward-propagating intraseasonal events in the simulation. Contours are the same as in Fig. 2.

of precipitation as seen from Fig. 7, which shows the time evolution of model-simulated precipitation averaged between 105° and 122°E. Comparing Fig. 7 with the corresponding observation in Fig. 2, we can see that the model simulated most of the precipitation events associated with the synoptic frontal systems, both southward propagating cold frontal systems and the quasi-stationary mei-yu fronts. Consistent with the spatial distribution of precipitation in July, the model underestimated precipitation associated with several synoptic events in later July in south China and Yangtze River basin between 20° and 32°N (comparing Figs. 2 and 7).

Figures 8 and 9 show the observed and simulated daily precipitation and their spatial standard deviations, respectively, for the three regions between 105° and 122°E over southern China (20°–26°N), Yangtze River basin (26°–32°N), and northern China (32°–40°N), as defined in Fig. 5. The model reproduced realistically the trends and fluctuations of precipitation over the three regions, except for an underestimation of both daily precipitation and its spatial variability in later July and early August over south China (Figs. 8a and 9a) and in Yangtze River basin (Figs. 8b and 9b). These underestimations are responsible for the bias in monthly mean daily rainfall shown in Fig. 6. This demonstrates that in order to realistically simulate the monthly mean precipitation, the model should be able to simulate reasonably well most of the individual precipitation events. Therefore, weather and climate are not necessarily separable, especially in the sense of high-resolution spatial distribution and temporal evolution.

To further quantify the model performance in simulation of precipitation, we calculated the statistics for simulated precipitation (Table 1), including the observed and simulated monthly mean daily precipitation, model bias, spatial pattern correlation coefficient (SC), and temporal correlation coefficient (CT) between the observed and simulated precipitations in the 4 months for the three regions as shown in Figs. 7 and 8. The model overestimated (positive bias) the area-averaged
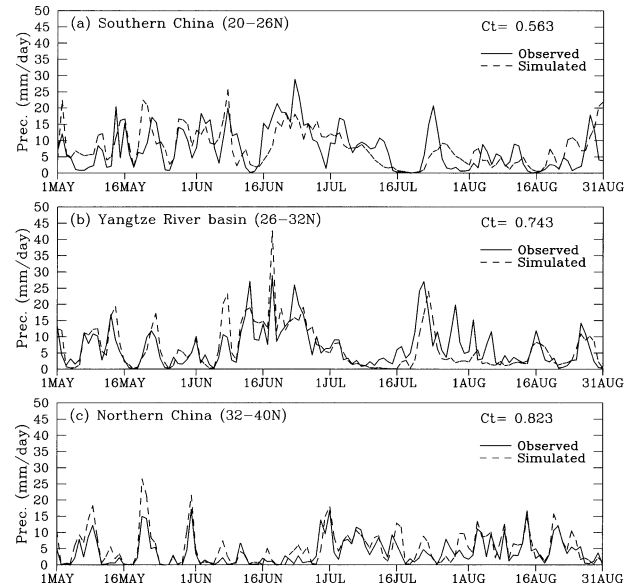

FIG. 8. The observed (solid) and model-simulated (dashed) areal-averaged daily precipitation in the 4 months for the three regions as defined in Fig. 5: (a) south China, (b) Yangtze River basin, (c) north China.

monthly mean precipitation in May in the three regions, an excess of about 44% in south China, 20% in the Yangtze River basin, and 64% in north China. These biases actually reduced in the later months, indicating that the model spinup time probably was too short to reflect the land surface processes and the associated forcing. The model, however, underestimated the precipitation in July in the Yangtze River basin by about
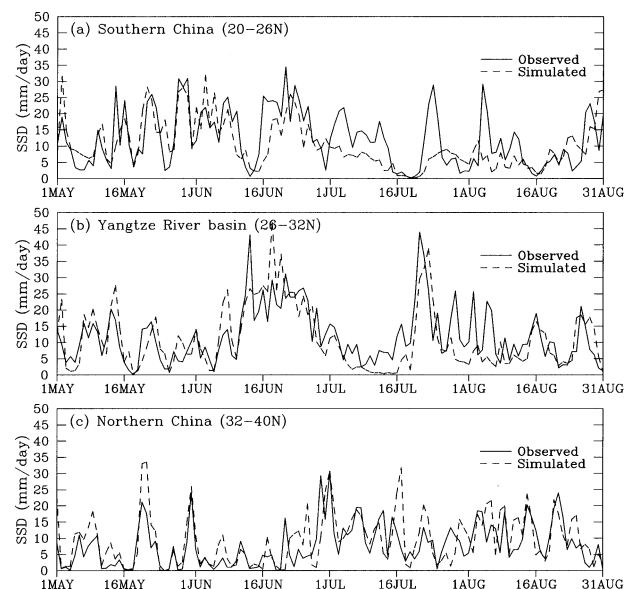

FIG. 9. Observed (solid) and model-simulated (dashed) spatial standard deviation of daily precipitation in the 4 months for the three regions as defined in Fig. 5.

TABLE 1. Monthly mean statistics of observed and simulated precipitation (mm day^{-1}) over the three regions in the 4 months.

Month	Region	Observed (mm)	Estimated (mm)	SC	CT	Bias (mm)
May	20°–26°N, 105°–122°E	6.90	9.91	0.268	0.594	3.01
	26°–32°N, 105°–122°E	5.37	6.45	0.223	0.829	1.08
	32°–40°N, 105°–122°E	3.75	6.17	0.737	0.966	2.42
Jun	20°–26°N, 105°–122°E	12.18	11.01	0.274	0.599	−1.17
	26°–32°N, 105°–122°E	10.57	12.49	0.796	0.786	1.92
	32°–40°N, 105°–122°E	2.06	2.72	0.364	0.555	0.66
Jul	20°–26°N, 105°–122°E	6.54	5.20	0.411	0.553	−1.34
	26°–32°N, 105°–122°E	7.25	4.32	0.214	0.676	−2.93
	32°–40°N, 105°–122°E	5.09	6.11	0.364	0.666	1.02
Aug	20°–26°N, 105°–122°E	4.19	6.02	0.393	0.287	1.83
	26°–32°N, 105°–122°E	4.61	3.96	0.662	0.521	−0.65
	32°–40°N, 105°–122°E	5.03	6.16	0.535	0.825	1.13

40%. This is due to the fact that the model underestimated the precipitation during the second mei-yu period in this region, as indicated above. The spatial pattern correlation coefficient for precipitation indicates reasonable skill in the 4 months, in particular, in June 79.6% was achieved over the Yangtze River basin. However, the simulated spatial pattern correlation coefficient was relatively lower in May for both the south China region (26.8%) and Yangtze River basin (22.3%), in June for south China (27.4%), and in July for Yangtze River basin (21.4%). The temporal correlation coefficient shows high correlation between the simulated and observed precipitations in all three regions (over 50%), except for a relatively lower correlation coefficient in August for the south China region (28.9%). Overall, in the 4 months, the temporal correlation coefficient increases with increasing latitude (56% for south China, 74% for Yangtze River basin, and 82% for north China), indicating that the tropical systems are harder to simulate compared with midlatitude systems.

In order to examine the model's capability in simulating the frequency of severe precipitation events, we show in Fig. 10 both the observed (left panels) and model simulated (right panels) horizontal distributions of frequency of occurrence for rainfall intensity larger than 10 (top), 30 (middle), and 50 (bottom) mm day^{-1}, respectively, during the 4 months. We can see that the model is able to reproduce the frequency distribution reasonably well, especially for the severe precipitation events. The model slightly underestimated the frequency of less intense precipitation events in the Yangtze River basin (Fig. 9b), which was due to the missing of several precipitation events in later July and early August as already seen in Figs. 7 and 8. In particular, the model reproduced the distribution of precipitation frequency quite well in June (Fig. 11) except for a small overestimation over the Yangtze River basin for rainfall intensity larger than 10 mm day^{-1} (Fig. 11b). To give an overall quantitative evaluation of the model's ability in reproducing the precipitation intensity frequency distribution, we show in Table 2 the spatial correlation coefficient between the observed and model-simulated frequency distribution based on the above three daily

rainfall intensity categories at all the land points in the domain shown in Fig. 10 for the whole 4 months and also for each individual month. It is clear that the model has a quite good skill in reproducing the spatial distribution of frequency of occurrence for the three rainfall intensity categories. Consistent with the above analyses, relatively lower skills occurred for July. The trend of decreasing in the spatial correlation coefficient with increasing the rainfall intensity threshold is due to the fact that the calculated correlation coefficient becomes more sensitive to the small shift in frequency distribution because of the small sampling at the extreme end of precipitation. Overall, however, the IPRC-RegCM appears to be able to simulate the frequency distribution for extreme precipitation events reasonably well. This is a prerequisite for a regional climate model used for either study of climate sensitivity or assessment of regional impact of global climate change.

It is also interesting to examine the partitioning between the subgrid-scale convective precipitation and grid-resolved precipitation. Figure 12 shows this partitioning of daily precipitation in the 4 months for the three regions. In the southern region, subgrid-scale convective precipitation was dominated, especially in the last two summer months (Fig. 12a), indicating active convective weather systems in the tropical and subtropical monsoon flow. In both the Yangtze River basin and the northern region, however, the grid-scale precipitation was dominated in the first 2 months (Fig. 12c), indicating large-scale precipitation associated with cold frontal systems in the premonsoon season. During the heavy rainfall mei-yu periods, the rainfall was dominated by the grid-resolved precipitation in the Yangtze River basin (Fig. 12b). This demonstrates that rainfall associated with the quasi-stationary mei-yu fronts over the Yangtze River basin was less convective in our simulation, consistent with previous simulation studies (e.g., Chen et al. 1998).

b. Monsoon circulation and vertical structure of the atmosphere

We have briefly discussed the observed onset and evolution of the 1998 East Asian summer monsoon in
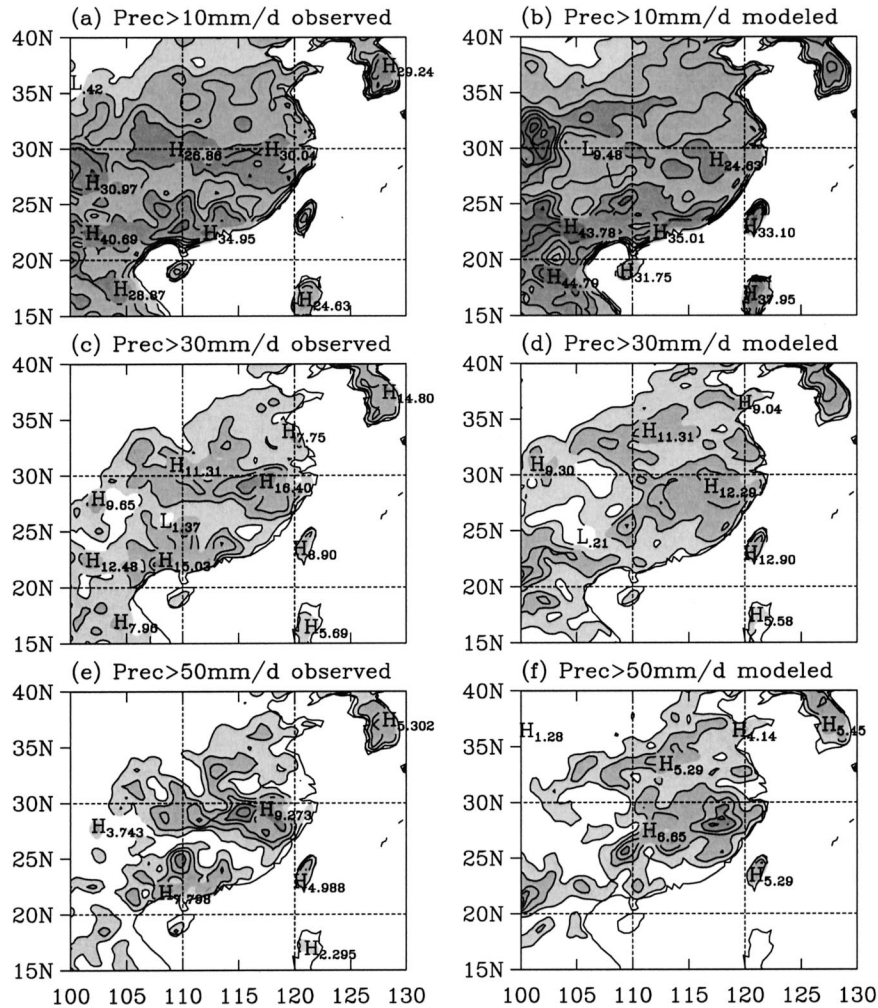
FIG. 10. (a), (c), (e) Observed and (b), (d), (f) model-simulated distributions of frequency of occurrence (percent in days during the 4 months) of daily rainfall larger than (a), (b) 10, (c), (d) 30, and (e), (f) 50 mm day^{-1}. Contours are 5% in (a) and (b), 3% in (c) and (d), and 1.5% in (e) and (f).

section 3. In order to see the ability of the model in simulating the monsoon flow, we show in Fig. 13 the simulated zonal, meridional wind speeds, and equivalent temperature at 850 hPa averaged between 110° and 120°E, the same as in Fig. 3. The model simulated the low-level monsoon flow quite realistically. In comparison with the low-resolution ECMWF analysis counterpart shown in Fig. 3, the model produced stronger monsoon flow, indicating high-resolution spatial structure and temporal variability. Note that the easterly flow in the southern region of the domain is stronger than the ECMWF analysis (Fig. 13a), implying that the model simulated stronger subtropical high over the western Pacific along the southeast China coast, especially in the last 2 months (not shown). Note that the model simulated two northward-propagating intraseasonal events reasonably well except that the westerly associated with the second intraseasonal event was missing

during 10–15 July (Figs. 3a and 13a) over the northern part of SCS (around 15°–20°N). This missing westerly concurred with the underestimation of precipitation during this period (Figs. 2 and 7) over south China (Figs. 1 and 6). The simulated meridional wind is quite similar to the ECMWF analysis (Fig. 13b). The equivalent temperature in SCS (south of 22°N) is lower than that in the ECMWF analysis (Fig. 13c). This cold bias over SCS is responsible for both the cold bias in minimum surface air temperature in south China and the underestimation of precipitation during the second mei-yu period in the Yangtze River basin in July (Fig. 6) since the air in this region is mostly originated from SCS. In the upper troposphere (Fig. 14), both the upper westerly jet and the easterly flow to the south are also well simulated but with a slightly stronger amplitude. Degrading model results to 2.5° by 2.5° resolution as the same as the driving fields gives more resemblance to the driving
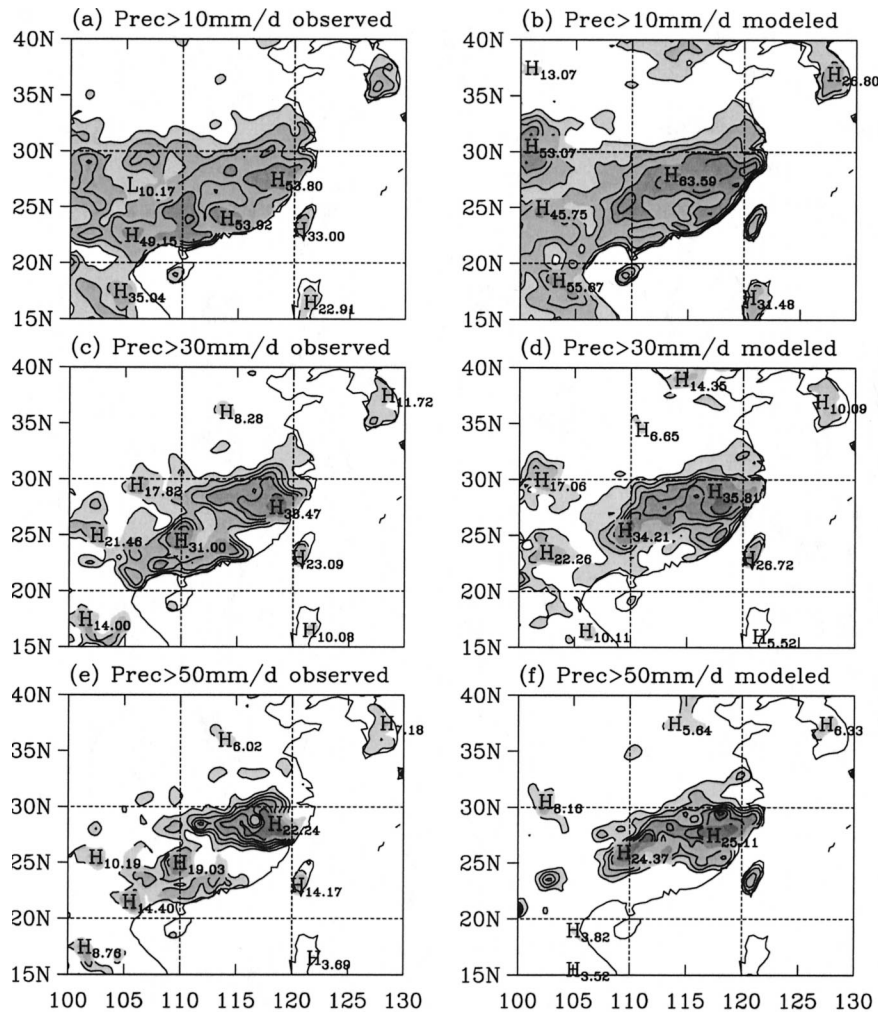
FIG. 11. As in Fig. 10 but only during Jun.

fields than those shown in Figs. 13 and 14 (not shown), indicating that the model does preserve the large-scale forcing in the computational domain.

In general, the IPRC-RegCM simulated the vertical structure of the atmosphere reasonably well. Figures 15 and 16 show the biases of water vapor mixing ratio and air temperature calculated for all model sigma levels in the 4 months for the three regions. We see that biases

TABLE 2. Spatial correlation coefficient between the model-simulated and observed frequency distribution for three daily rainfall (Prec) categories (larger than 10, 30, and 50 mm day^{-1}, respectively) at the land points as shown in Fig. 10 in the 4 months and in the whole May–Aug 123 days.

Month	Prec $\geq$ 10 mm day^{-1}	Prec $\geq$ 30 mm day^{-1}	Prec $\geq$ 50 mm day^{-1}
May	0.491	0.350	0.269
Jun	0.749	0.647	0.585
Jul	0.382	0.255	0.204
Aug	0.531	0.362	0.282
May–Aug	0.584	0.500	0.475

are generally between -1.5 and 1.0 g kg^{-1} for water vapor mixing ratio and between $-1.0°$ and $1.0°$C for air temperature, respectively. Note that the largest dry bias occurred in a deep layer through the troposphere in the south China region and in Yangtze River basin in July (Fig. 15). This is consistent with the underestimation of rainfall in the two regions in this month (Fig. 6). Bias in air temperature shows a persistent cold bias in the mid-lower troposphere in the south China region during the 4 months, especially in July and August (Fig. 16). A similar, but smaller, midlevel cold bias also occurred for Yangtze River basin in June–August.

Three possible causes might be responsible for the cold and dry biases in the lower troposphere over SCS and the southern China region, as also seen from the equivalent temperature given in Fig. 11c. One is the uncertainties in calculating the sea surface sensible and latent heat fluxes in the model, which are accomplished using the TOGA COARE algorithm (Fairall et al. 1996). The applicability of this algorithm to SCS has not been verified. The second possible cause is the subgrid cu-
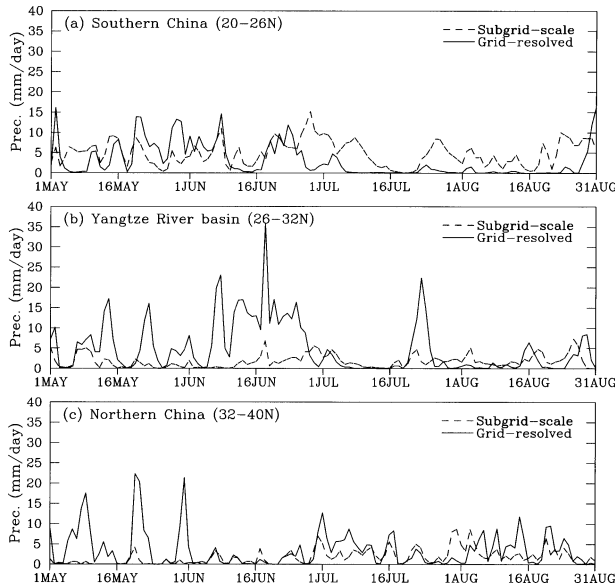
FIG. 12. Simulated areal-averaged daily subgrid convective precipitation (dashed) and grid-resolved precipitation (solid) in the 4 months for the three regions as defined in Fig. 5.

FIG. 13. As in Fig. 3 but from model simulation.

mulus parameterization. As noticed already by Giorgi et al. (1993b), some of schemes could produce cold and dry bias in the lower troposphere probably due to the uncertainties in parameterization of downdrafts. The third possible cause may be the intrinsic low predictability of the atmospheric motion in the Tropics as indicated by McGregor (1997) and its downstream effect to the south of the Yangtze River. Other possible factors include the uncertainties in the driving fields that provide the lateral boundary conditions but with no cloud information and the uncertainties in model physics parameterizations associated with the feedback among cloud, radiation, and land surface processes. Further studies are required to further identify the actual sources responsible for the model bias. Nevertheless, the biases in our model are comparable to, or even less than, those found in some other regional climate models in the same region (e.g., Leung et al. 1999; Sasaki et al. 2000; Wang et al. 2000).
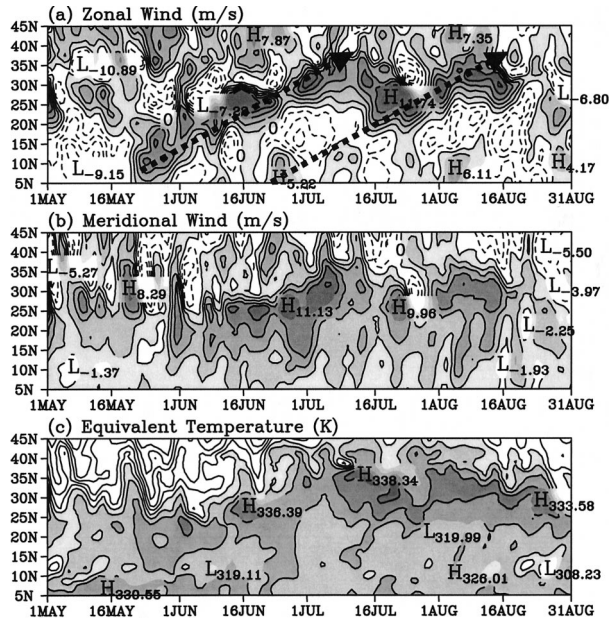
c. Surface air temperature and relative humidity

To compare the model simulated with observed surface air (2 m above the surface) temperatures, we used the approximation suggested by Dickinson et al. (1993) to estimate the simulated surface air temperature

$$T_a = 0.55T_m + 0.45T_f, \qquad (9)$$

where T_m is the air temperature at the lowest model level, and T_f the air temperature within the foliage canopy if vegetation is present or the ground temperature if the surface is bare soil.

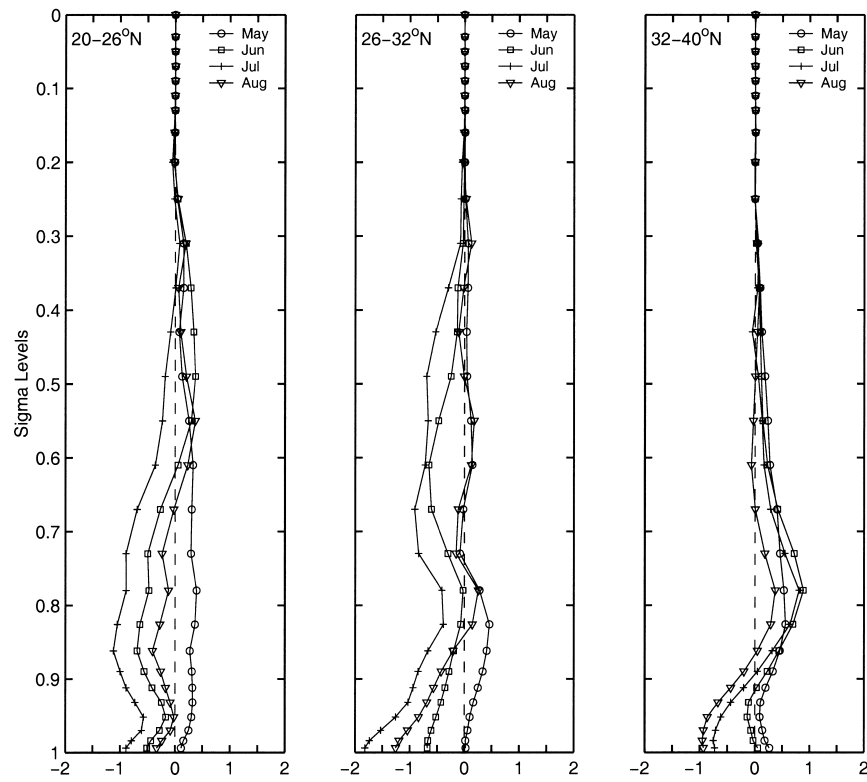To demonstrate the overall performance of the coupled land–atmospheric regional model in simulating the

observed variation, we show in Fig. 17 the area-averaged daily maximum (a) and minimum (b) surface air temperatures in the 4 months for the three regions defined in Fig. 5. In general, the model captured the trends in both maximum and minimum surface air temperatures in the three regions except for a consistent cold bias (less than 2°C) in daily minimum surface air temperature during the last 2 months in the southern China region (Fig. 17a) and a warm bias (about 1°–3°C) in maximum surface air temperature in the northern China region (Fig. 17c). Both cold and warm biases of surface air temperature are consistent with bias in air temperature (Fig. 15).

Figure 18 gives the model-simulated and observed daily maximum and minimum relative humidities of the surface air. Although the model reproduced the trends of both daily maximum and minimum in relative humidity of surface air, it underestimated the daily minimum relative humidity during the daytime in comparison with the observations. This underestimation in surface air relative humidity during the daytime can be explained partly by the warm bias in maximum surface air temperature, which gives higher saturation mixing ratio and thus a lower relative humidity for a given water vapor mixing ratio. However, the major cause of the

FIG. 14. As in Fig. 4 but from model simulation.

FIG. 15. Vertical profile of bias in water vapor mixing ratio (g kg^{-1}) in the 4 months averaged in three regions as defined in Fig. 5.
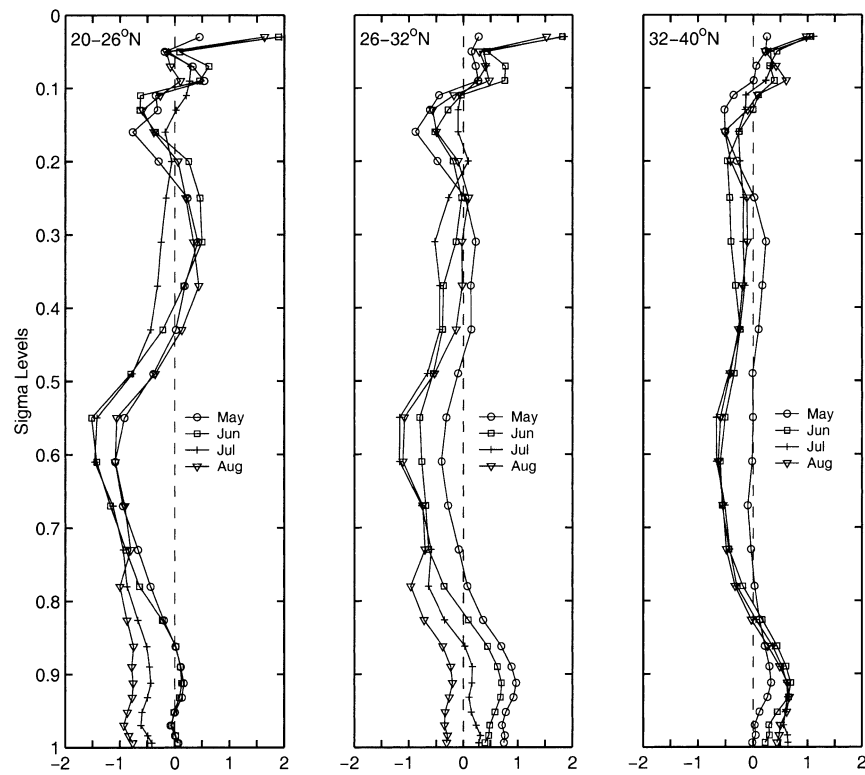

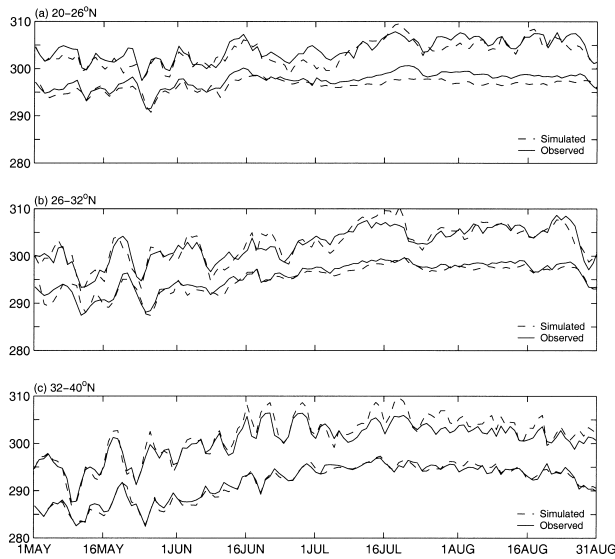FIG. 16. As in Fig. 15 but for air temperature (°C).

FIG. 17. Observed (solid) and model-simulated (dashed) daily minimum (lower curves in each panel) and maximum (upper curves in each panel) surface (2-m height) air temperatures (°C) averaged in the three regions as defined in Fig. 5 from 1 May to 31 Aug 1998.
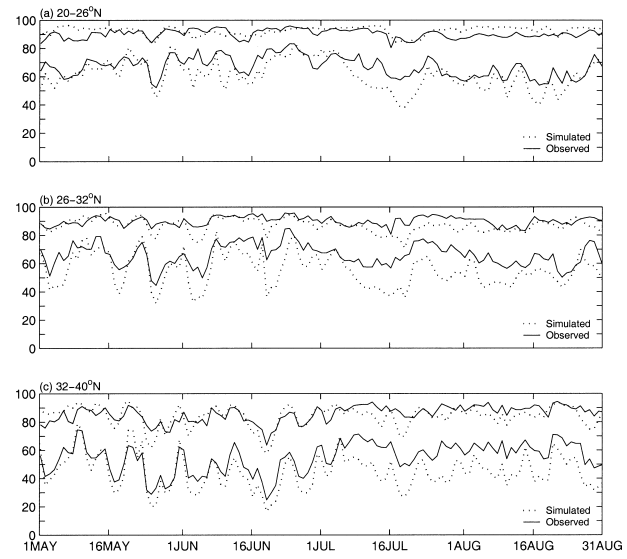

FIG. 18. As in Fig. 15 but for daily minimum (during daytime, lower curve in each panel) and maximum (during nighttime, upper curve in each panel) relative humidity (%) in the surface air at 2-m height.

underestimation in relative humidity was the dry bias in water vapor mixing ratio in the lower troposphere (Fig. 16).

6. Summary and concluding remarks

In this paper, the regional climate model, IPRC-RegCM, recently developed at the International Pacific Research Center has been described in detail. Although similar to some other available regional climate models in many aspects, this model has several distinct features. These include the direct feedback of cloud water–ice detrained from the top of cumulus cloud towers into the grid-resolved quantities; the effect of mixed-ice phase cloud buoyancy on turbulence production; an explicit coupling between the cloud microphysics and radiation via cloud properties; an explicit coupling between land surface and radiation via surface albedo, direct, and diffuse radiation fluxes; and the inclusion of frictionally generated dissipative heating. These features make the model highly resolvable and can simulate a wide range of scales and scale interactions. The model is highly vectorized and also parallelized, thus very efficient to run.

The capability of the model in simulating regional climate has been demonstrated with its simulation of the 1998 severe precipitation event over China. With the ECMWF analysis available at 12-h intervals with 2.5° × 2.5° resolution as both initial and lateral boundary conditions, the IPRC-RegCM successfully simulated the 1998 severe precipitation event in the Yangtze River basin over China during the summer monsoon season. The results from a 4-month-long simulation show that the model reproduced realistically not only

the temporal evolution of the area-averaged precipitation and the monthly mean precipitation spatial pattern but also the daily precipitation intensity distribution. This latter is desirable for a regional climate model to be used for either studying the sensitivity of the climate system to various physical processes and different external forcings or assessing regional impact of global climate change. The model also reproduced the monsoon flow quite well, especially the activities of two episodes of northward-propagating intraseasonal oscillation events, which are believed to be closely related to the unusual double mei-yu periods in the Yangtze River basin over China in 1998.

Although the overall model performance is encouraging, there exist some persistent biases, such as a cold bias in the minimum surface air temperature in the southern China region and a warm bias in the maximum surface air temperature in the northern China region. The model also has a dry bias in minimum relative humidity of the surface air during the daytime, especially in July over the Yangtze River basin and in both July and August in the northern China region. The model also overestimated the precipitation in the first month, seemingly due to a too short time spinup of the land surface processes, which usually takes about several months or even longer to reach an equilibrium (Christensen 1999). In addition, the model only reproduced about 60% of the observed rainfall amount and with main rainbelt displaced about 2° latitudes to the north during the unusual second mei-yu period in the Yangtze River basin. Among several possible causes responsible for this significant bias, the most likely cause could be the fact that the easterly south of 30°N was dominated in the simulation, but the westerly was dominated in

observation, during July and early August (Figs. 3 and 13), implying a stronger subtropical high ridge over south China (between 20° and 25°N) in the simulation. This subtropical ridge played a role in reducing the moisture transport from the southwest monsoon flow and thus reduced the rainfall over the Yangtze River basin in later July and early August in both the south China region and Yangtze River basin (Figs. 8a,b).

Previous studies revealed the possible effect of domain location, size, and the width of buffer zone on regional climate simulations (e.g., Seth and Giorgi 1998; Gong and Wang 2000; Liang et al. 2001). To further identify the causes that are responsible for our model biases, we will study the sensitivity of the model simulation to various processes and parameter spaces, such as the parameterization of cumulus convection, domain location and size, width of buffer zone, etc. in a companion paper. Meanwhile, ensemble simulation with different initial dates will be also conducted to identify the systematic errors in the simulation since the ensemble technique can remove those biases related to the chaotic behavior of the atmospheric internal dynamics. In addition, only one extremely wet case has been simulated with our IPRC-RegCM. More cases will be simulated in order to identify systematic errors and to improve the model physics, and thus to make the model a useful tool for supporting our regional climate research.

APPENDIX

Objective Measures of Model Performance

As indicated in section 3, we used several objective statistics to measure the model performance and to verify the model simulation. The primary measure of simulation skill is the model bias Er defined as

$$Er = \frac{1}{N} \sum_i \sum_j (a_{i,j}^m - a_{i,j}^o), \qquad (A1)$$

where N is the total number of grid points within a given region; subscripts i, j are the horizontal gridpoint indices in the zonal and meridional directions, respectively; a

can be any meteorological parameters either daily mean or monthly mean; superscripts m and o refer to the observed and model simulated quantities, respectively.

The spatial correlation coefficient between simulated and observed quantity a is defined as

$$SC = \frac{\sum_i \sum_j (a_{i,j}^m - \overline{a_{i,j}^m})(a_{i,j}^o - \overline{a_{i,j}^o})}{\left[\sum_i \sum_j (a_{i,j}^m - \overline{a_{i,j}^m})^2 \sum_i \sum_j (a_{i,j}^o - \overline{a_{i,j}^o})^2\right]^{1/2}}, \qquad (A2)$$

where the overbar denotes spatial averaging.

The temporal correlation coefficient (CT) between simulated and observed quantity a is defined as

$$CT = \frac{\sum_n (a_n^m - \overline{a_n^m})(a_n^o - \overline{a_n^o})}{\left[\sum_n (a_n^m - \overline{a_n^m})^2 \sum_n (a_n^o - \overline{a_n^o})^2\right]^{1/2}}, \qquad (A3)$$

where the overbar denotes time mean.

The spatial standard deviation (SSD) of a variable a is defined as

$$SSD = \left[\frac{\sum_i \sum_j (a_{i,j} - \overline{a_{i,j}})^2}{(M-1) \times (N-1)}\right]^{1/2}, \qquad (A4)$$

where the overbar denotes the spatial averaging, and M, N the numbers of total grid points in the zonal and meridional directions, respectively.

REFERENCES

Bister, M., and K. A. Emanuel, 1998: Dissipative heating and hurricane intensity. *Meteor. Atmos. Phys.,* **55,** 233–240.

Bosilovich, M. G., and W.-Y. Sun, 1999: Numerical simulation of the 1993 Midwestern flood: Land–atmosphere interactions. *J. Climate,* **12,** 1490–1505.

Caya, D., and R. Laprise, 1999: A semi-implicit semi-Lagrangian regional climate model: The Canadian RCM. *Mon. Wea. Rev.,* **127,** 341–362.

Chen, S.-J., Y.-H. Kuo, W. Wang, Z.-Y. Tao, and B. Cui, 1998: A modeling case study of heavy rainstorm along the Mei-yu front. *Mon. Wea. Rev.,* **126,** 2330–2351.

Chou, M., M. J. Suarez, C.-H. Ho, M. M.-H. Yan, and K.-T. Lee, 1998: Parameterizations for cloud overlapping and shortwave single-scattering properties for use in general circulation and cloud ensemble models. *J. Climate,* **11,** 202–214.

Christensen, J. H., 1999: Relaxation of soil variables in a regional climate model. *Tellus,* **51A,** 474–685.

——, B. Machenhauer, R. G. Jones, C. Schar, P. M. Ruti, M. Castro, and G. Visconti, 1997: Validation of present day regional climate simulations over Europe: LAM simulations with observed boundary conditions. *Climate Dyn.,* **13,** 489–506.

Detering, H. W., and D. Etling, 1985: Application of the E-ϵ turbulence model to the atmospheric boundary layer. *Bound.-Layer Meteor.,* **33,** 113–133.

Dickinson, R. E., R. M. Errico, F. Giorgi, and G. T. Bates, 1989: A regional climate model for the western U.S. *Climate Change,* **15,** 383–422.

——, A. Henderson-Sellers, and P. J. Kennedy, 1993: Biosphere–atmosphere transfer scheme (BATS) version 1 as coupled to the

NCAR Community Climate Model. NCAR Tech. Note NCAR/TN-387+STR, National Center for Atmospheric Research, Boulder, CO, 72 pp.

Ding, Y.-H., 1994: *Monsoons over China.* Kluwer Academic, 419 pp.

——, and Y. Liu, 2001: Onset and the evolution of the summer monsoon over the South China Sea during SCSMEX Field Experiment I 1998. *J. Meteor. Soc. Japan,* **79,** 255–276.

Dudek, M. P., X.-Z. Liang, and W.-C. Wang, 1996: A regional climate model study of the scale dependence of cloud–radiation interactions. *J. Climate,* **9,** 1221–1234.

Edwards, J. M., and A. Slingo, 1996: Studies with a flexible new radiation code. I: Choosing a configuration for a large-scale model. *Quart. J. Roy. Meteor. Soc.,* **122,** 689–719.

Fairall, C. W., E. F. Bradley, D. P. Rogers, J. B. Edson, and G. S. Young, 1996: Bulk parameterization of air–sea fluxes for Tropical Ocean–Global Atmosphere Coupled Ocean Atmosphere Response Experiment. *J. Geophys. Res.,* **101,** 3747–3764.

Fowler, L. D., and D. A. Randall, 1996: Liquid and ice cloud microphysics in the CSU general circulation model. Part II: Impact on cloudiness, the earth's radiation budget, and the general circulation of the atmosphere. *J. Climate,* **9,** 530–560.

Giorgi, F., 1990: Simulation of regional climate using a limited area model nested in a general circulation model. *J. Climate,* **3,** 941–963.

——, and G. T. Bates, 1989: The climatological skill for a regional model over complex terrain. *Mon. Wea. Rev.,* **117,** 2325–2347.

——, and L. O. Mearns, 1991: Approaches to the simulation of regional climate change: A review. *Rev. Geophys.,* **29,** 191–216.

——, and ——, 1999: Introduction to special section: Regional climate modeling revisited. *J. Geophys. Res.,* **104,** 6335–6352.

——, M. R. Marinucci, and G. T. Gates, 1993a: Development of a second-generation regional climate model (RegCM2). Part I: Boundary-layer and radiative transfer processes. *Mon. Wea. Rev.,* **121,** 2794–2813.

——, ——, ——, and G. DeCanio, 1993b: Development of a second-generation regional climate model (RegCM2). Part II: Convective processes and assimilation of lateral boundary conditions. *Mon. Wea. Rev.,* **121,** 2814–2832.

——, L. O. Mearns, C. Shields, and L. Mayer, 1996: A regional model study of the importance of local versus remote controls of the 1988 drought and the 1993 flood over the central United States. *J. Climate,* **9,** 1150–1162.

Gong, W., and W.-C. Wang, 2000: A regional model simulation of the 1991 severe precipitation event over the Yangtze–Huai River Valley. Part II: Model bias. *J. Climate,* **13,** 93–108.

Heymsfield, A. J., and L. J. Donner, 1990: A scheme for parameterizing ice-cloud water content in general circulation models. *J. Atmos. Sci.,* **47,** 1865–1877.

Holland, G. J., 1995: Scale interaction in the western Pacific monsoon. *Meteor. Atmos. Phys.,* **56,** 57–79.

Hong, S.-Y., H.-M. H. Juang, and Q. Zhao, 1998: Implementation of prognostic cloud scheme for a regional spectral model. *Mon. Wea. Rev.,* **126,** 2621–2639.

——, ——, and D.-K. Lee, 1999: Evaluation of a regional spectral model for the East Asian monsoon case studies for July 1987 and 1988. *J. Meteor. Soc. Japan,* **77,** 553–572.

Houghton, J. T., Y. Ding, D. J. Griggs, M. Noguer, P. J. van der Linden, X. Dai, K. Maskell, and C. A. Johnson, Eds., 2001: *Climate Change 2001: The Scientific Basis.* Cambridge University Press, 881 pp.

Jones, R. G., J. M. Murphy, and M. Noguer, 1995: Simulation of climate change over Europe using a nested regional-climate model. Part I: Assessment of control climate, including sensitivity to location of boundaries. *Quart. J. Roy. Meteor. Soc.,* **121,** 1413–1450.

Kang, I.-S., and Coauthors, 2002: Intercomparison of the climatological variations of Asian summer monsoon precipitation simulated by 10 GCMs. *Climate Dyn.,* **19,** 383–395.

Kida, H., T. Koide, H. Sasaki, and M. Chiba, 1991: A new approach to coupling a limited area model with a GCM for regional climate simulations. *J. Meteor. Soc. Japan,* **69,** 723–728.

Lee, D.-K., and M.-S. Suh, 2000: Ten-year Asian summer monsoon simulation using a regional climate model (RegCM2). *J. Geophys. Res.,* **105,** 29 565–29 577.

Leung, L. R., S. J. Ghan, Z.-C. Zhao, Y. Luo, W.-C. Wang, and H.-L. Wei, 1999: Intercomparison of regional climate simulations of the 1991 summer monsoon in eastern Asia. *J. Geophys. Res.,* **104,** 6425–6454.

Liang, X.-Z., K. E. Kunkel, and A. N. Samel, 2001: Development of a regional climate model for U.S. Midwest application. Part I: Sensitivity to buffer zone treatment. *J. Climate,* **14,** 4363–4378.

Liu, Y.-Q., F. Giorgi, and W. M. Washington, 1994: Simulation of summer monsoon climate over East Asia with an NCAR regional climate model. *Mon. Wea. Rev.,* **122,** 2331–2348.

——, R. Avissar, and F. Giorgi, 1996: Simulation with the regional climate model RegCM2 of extremely anomalous precipitation during the 1991 East Asian flood: An evaluation study. *J. Geophys. Res.,* **101,** 26 199–26 216.

McGregor, J. L., 1997: Regional climate modeling. *Meteor. Atmos. Phys.,* **63,** 105–117.

——, and K. Walsh, 1994: Climate change simulations of Tasmanian precipitation using multiple nesting. *J. Geophys. Res.,* **99,** 20 889–20 905.

Nordeng, T. E., 1995: Extended versions of the convective parameterization scheme at ECMWF and their impact on the mean and transient activity of the model in the Tropics. ECMWF Research Department Tech. Memo. 206, 41 pp.

Paegle, J., K. C. Mo, and J. N. Paegle, 1996: Dependence of simulated precipitation on surface evaporation during the 1993 United States summer floods. *Mon. Wea. Rev.,* **124,** 345–361.

Pal, J. S., and E. A. B. Eltahir, 2001: Pathways relating soil moisture conditions to future summer rainfall within a model of the land–atmosphere system. *J. Climate,* **15,** 1227–1242.

Pan, Z., M. Segal, R. Turner, and E. Takle, 1995: Model simulation of impacts of transient surface wetness on summer rainfall in the United States Midwest during drought and flood years. *Mon. Wea. Rev.,* **123,** 1575–1581.

Petch, J. C., 1998: Improved radiative transfer calculations from information provided by bulk microphysical schemes. *J. Atmos. Sci.,* **55,** 1846–1858.

Polcher, J., and Coauthors, 1998: A proposal for a general interface between land surface schemes and general circulation models. *Global Planet. Change,* **19,** 261–276.

Randall, D. A., 1995: Parameterizing fractional cloudiness produced by cumulus entrainment. Preprints, *Workshop on Cloud Microphysics Parameterizations in Global Atmospheric Circulation Models,* Kananaskis, AB, Canada, WMO, 1–16.

Renwick, J. A., J. J. Katzfey, K. C. Nguyen, and J. L. McGregor, 1998: Regional model simulations of New Zealand climate. *J. Geophys. Res.,* **103D,** 5973–5982.

Reynolds, R. W., and T. M. Smith, 1994: Improved global sea surface temperature analyses using optimum interpolation. *J. Climate,* **7,** 929–948.

Rockel, B., E. Raschke, and B. Weyres, 1991: A parameterization of broad band radiative transfer properties of water, ice and mixed clouds. *Beitr. Phys. Atmos.,* **64,** 1–12.

Roeckner, E., and Coauthors, 1996: The atmospheric general circulation model ECHAM-4: Model description and simulation of present-day climate. Max-Planck-Institut für Meteorologie, Rep. 218, Hamburg, Germany, 90 pp.

Sasaki, H., Y. Sato, K. Adachi, and H. Kida, 2000: Performance and evaluation of the MRI regional climate model with the spectral boundary coupling method. *J. Meteor. Soc. Japan,* **78,** 477–489.

Schär, C., D. Lüthi, and U. Beyerle, 1999: The soil–precipitation feedback: A process study with a regional climate model. *J. Climate,* **12,** 722–741.

Seth, A., and F. Giorgi, 1998: The effects of domain choice on summer precipitation simulation and sensitivity in a regional climate model. *J. Climate,* **11,** 2698–2712.

Slingo, A., and H. M. Schrecker, 1982: On the shortwave radiative properties of water clouds. *Quart. J. Roy. Meteor. Soc.,* **108,** 407–426.

Sun, Z., and K. Shine, 1994: Studies of the radiative properties of ice and mixed phase clouds. *Quart. J. Roy. Meteor. Soc.,* **120,** 111–137.

——, and L. Rikus, 1999: Improved application of exponential sum fitting transmissions to inhomogeneous atmosphere. *J. Geophys. Res.,* **104D,** 6291–6303.

Tiedtke, M., 1989: A comprehensive mass flux scheme for cumulus parameterization in large-scale models. *Mon. Wea. Rev.,* **117,** 1779–1800.

Walsh, K., and J. L. McGregor, 1995: January and July climate simulations over the Australian region using a limited-area model. *J. Climate,* **8,** 2387–2403.

Wang, B., and X. Xu, 1997: Northern Hemispheric summer monsoon singularities and climatological intraseasonal oscillation. *J. Climate,* **10,** 1071–1085.

——, and LinHo, 2002: Rainy season of the Asian–Pacific summer monsoon. *J. Climate,* **15,** 386–398.

Wang, W.-C., W. Gong, and H. Wei, 2000: A regional model simulation of the 1991 severe precipitation event over the Yangtze–Huai River Valley. Part I: Precipitation and circulation statistics. *J. Climate,* **13,** 74–92.

Wang, Y., 1999: A triply nested movable mesh tropical cyclone model with explicit cloud microphysics—TCM3. BMRC Research Rep. 74, Bureau of Meteorology Research Centre, Australia, 81 pp.

[Available from Bureau of Meteorology Research Centre, Melbourne, Australia, VIC 3001.]

——, 2001: An explicit simulation of tropical cyclones with a triply nested movable mesh primitive equation model—TCM3. Part I: Model description and control experiment. *Mon. Wea. Rev.,* **129,** 1370–1394.

——, 2002a: An explicit simulation of tropical cyclones with a triply nested movable mesh primitive equation model—TCM3. Part II: Model refinements and sensitivity to cloud microphysics parameterization. *Mon. Wea. Rev.,* **130,** 3022–3036.

——, 2002b: Vortex Rossby waves in a numerically simulated tropical cyclone. Part I: Overall structure, potential vorticity, and kinetic energy budgets. *J. Atmos. Sci.,* **59,** 1213–1238.

——, 2002c: Vortex Rossby waves in a numerically simulated tropical cyclone. Part II: The role in tropical cyclone structure and intensity changes. *J. Atmos. Sci.,* **59,** 1239–1262.

——, and B. Wang, 2001: Toward a unified highly resolved regional climate modeling system. *Present and Future of Modeling Global Environmental Change: Toward Integrated Modeling,* T. Matsuno and H. Kida, Eds., Terra Scientific, 29–48.

Xu, K.-M., and D. A. Randall, 1996: A semiempirical cloudiness parameterization for use in climate models. *J. Atmos. Sci.,* **53,** 3084–3102.

Xue, M., and S.-J. Lin, 2001: Numerical equivalence of advection in flux and advective forms and quadratically conservative high-order advection schemes. *Mon. Wea. Rev.,* **129,** 561–565.

Zhang, G.-J., 1994: Effects of cumulus convection on the simulated monsoon circulation in a general circulation model. *Mon. Wea. Rev.,* **122,** 2022–2038.